CFD Analysis of Hypersonic Flowfields with Surface Thermochemistry and Ablation

W. D. Henline *
NASA Ames Research Center, MS 230-2,
Moffett Field, CA 94035-1000

September 9, 1997

Abstract

In the past forty years much progress has been made in computational methods applied to the solution of problems in spacecraft hypervelocity flow and heat transfer. Although the basic thermochemical and physical modeling techniques have changed little in this time, several orders of magnitude increase in the speed of numerically solving the Navier-Stokes and associated energy equations have been achieved. The extent to which this computational power can be applied to the design of spacecraft heat shields is dependent on the proper coupling of the external flow equations to the boundary conditions and governing equations representing the thermal protection system in-depth conduction, pyrolysis and surface ablation phenomena. A discussion of the techniques used to do this in past problems as well as the current state-of-art is provided. Specific examples, including past missions such as Galileo, together with the more recent case studies of ESA/Rosetta Sample Comet Return, Mars Pathfinder and X-33 will be discussed. Modeling assumptions, design approach and computational methods and results are presented.

Nomenclature

$\tilde{D}_\alpha$	=	diffusivity for species α against the mean
$\underline{F}$	=	local body function (e.f. acceleration of gravity) for momentum eq.
h_1, h_2, h_3	=	flowfield metrics for body fixed coordinate system
h	=	static enthalpy
H_T	=	total flowfield enthalpy (static and kinetic energy)
$\underline{J}$	=	diffusive mass flux vector
k_T	=	thermal conductivity
P	=	local total pressure
$\underline{q}$	=	total heat flux vector
$\underline{q}^R$	=	total radiative heat flux vector
r	=	local radial distance to flowfield point (axisymmetric flow)
R	=	universal gas constant (equation of state)
R_α	=	gas phase volumetric reaction rate source term for species, α
s, n, t	=	streamwise, normal and tangential body fixed coordinate variables
T	=	temperature
$\underline{V}$	=	flowfield velocity vector
$\underline{v}$	=	flowfield velocity vector in body fixed coordinates
W	=	volumetric source term for total energy equation
u, v, w	=	velcity components along s,n,t coordinate directions in body fixed coordinate system
x, y, z	=	general rectangular cartesian coordinates
x_α	=	mass fraction for species α

Greek Symbols

κ	=	local surface metric or surface curvature function
μ	=	coefficient of viscosity
ρ	=	fluid mass density
τ	=	time variable
$\underline{\underline{\tau}}$	=	total stress tensor

Subscripts and Superscripts

α	=	reference to species "α"
g	=	gas phase
n	=	direction normal to wall
s	=	solid phase
ave	=	average

Introduction and Background

Whenever any spacecraft is placed in an orbit with a high enough energy state, its ultimate return to rest on the surface of a planetary body will result in the rapid dissipation of kinetic energy through either release of stored chemical energy (retro-rockets) or compressive and frictional drag forces due to an atmosphere. This latter situation is the object of the current discussion and

*Research Scientist, Reacting Flow Environments Branch, Senior Member AIAA.

represents the usual hypersonic re-entry physics problems prevalent in modern spacecraft heatshield design. This design issue has been with us since World War II when the German V-2 missile program first encountered pre-mature, in-flight warhead detonations which, after some head scratching, was correctly traced to aerothermodynamic heating of the nosecone during the high dynamic pressure portion of the V-2 trajectory. The solution at the time was to use readily available plywood as an ablative heatshield covering for the warhead. Obviously it worked! Things have progressed somewhat since then, but none of the underlying principles or problems have changed.

With the onset of the Cold War, development of ballistic missile technology provided a boost to activities in the theoretical aspects of hypersonic flight and heat transfer. Re-entry vehicles for these military missions experienced flight environments where peak dynamic pressures exceeded several tens of atmospheres and stagnation heat fluxes in the kilowatt range. To properly shape nosecones, to choose heat shield materials and to determine their thicknesses, adequate theoretical methods needed to be developed. The classic works of Lees[1], Fay and Riddell[2], Kemp, Rose and Detra[3] and Goulard[4] were the response to these analytical needs. These very early hypersonic flow and heat transfer methods were the initial basis for todays' modern real gas theoretical and flowfield solution techniques.

From the above discussion it is obvious that it is impossible to refer in any way to the issue of hypersonic flight and associated vehicle surface heating without reference to the specific re-entry trajectory and flight domain. The choice of theoretical modeling methods for the underlying fluids and thermophysics, as well as the analytical or numerical solution methods (including the proper CFD technique) are intimately related to the specific flight corridor under consideration. The entire approach is mission dependent. An example of the rather extreme variation in conditions and resultant phenomena which are thus generated can be ascertained from Figure 1. This composite plot of flight velocity, altitude and normal shock density ratio encompasses some of the primary missions NASA has flown within the Earth's atmosphere. As Earth entry velocities increase from 5 km/sec. up to orbital values of 7-8 km/sec, most flight bodies, e.g. Shuttle, NASP (as originally proposed) and the current proposed RLV (Re-usable Launch Vehicle) experience strong bow shock waves which, initially excite the vibrational modes of the constituent N_2 and O_2 molecules, and ultimately dissociate them into N and O to varying degrees depending on velocity and altitude. This, of course, is the source of the so-called "real gas" effects an accounting of which is necessary in the Navier-Stokes, energy and constituent species governing equations. The existence of dissociated gas species in the vehicle shock layer flow for these flights can also (depending on the specific heat shield material used) give rise to exothermic surface catalytic recombination reactions which further add to the surface heat transfer. Further increases in entry speed continue to excite additional energy exchange modes among the flowfield species including electronic state excitation, ionization and radiation events. In the range of 7-10 km/sec, such proposed missions as the Aeroassist Flight Experiment (AFE) and cargo carrying GEO to LEO return aerobraking missions begin to encounter these additional phenomena. At higher velocities, beyond 10 km/sec. past missions like Apollo and proposed Mars, Earth return entries result in increased levels of flowfield generated radiation and thermochemical ablative heating. The computation of these effects adds an additional element of complexity to both the thermophysical modeling as well as the numerical complexity of solving the necessary governing equations. Discussion of these latter issues is a main topic of this paper.

Finally, at the far end of the energy spectrum lie the very high speed comet and asteroid entry scenarios typified in Fig. 1 by the Pribram Meteor with entry velocities in excess of 20-30 km/sec. Very few attempts have been made to accurately simulate the flowfield and associated fluid physics for such severe entry problems. This is true regardless of the level of fidelity of the modeling. High speed asteroid entries involve radiation dominated flows at extreme enthalpy and pressure levels. Radiation events result from multiple levels of electronic exitation and several levels of ionization. Knowledge of the radiation cross-sections for these events do not yet exist. Pressure levels, although high, are not high enough to allow the usual radiation diffusion approximations possible with stellar radiation problems. Therefore a complete spectral treatment is required. To make matters worse, the resultant heat transfer and ablative response of the entry bolide is so severe that the induced thermal and mechanical stresses tend to cause deformation and breakup of the body. Modeling of such tightly coupled solid/flowfield behavior has not yet been attempted. To perform a first principles Navier-Stokes type CFD/radiation/ablation computation of this type amounts to one of the most difficult problems that can occur in both physics and computational science. Future research is obviously required to accurately solve such complex interactions.

The range of flight velocities experienced in hypersonic re-entry is very large and therefore results in a wide range of induced energy exchange phenomena. To accurately compute surface heating thus requires examination of the range of differences in flowfield behavior, transport phenomena, chemical reaction mechanisms and radiation physics which occur over these flight regimes. This is discussed in the following.

Flight Regimes and Flow Physics

In the above discussion surrounding Fig. 1, it is implicit that the proper governing equations are available

to solve the various problems possible in each flight regime. This is not actually the case, and some assumptions and restrictions are applied to constrain the problem. Figure 2 depicts the typical flight regimes which can occur under hypervelocity conditions. This plot also includes a density ratio for air (i.e. Earth entry) at the various velocity-altitudes encountered. As a re-ntry vehicle (RV) descends in altitude, the fluid mechanical behavior of the body's external flowfield will dramatically change. At the highest altitudes, densities are low enough such that only free molecular flow (no particle interaction) occurs. At slightly lower altitudes, atomic and molecular collisions are occurring but do not significantly affect the fluid dynamics (free collision regime). These flight regimes are called the "non-continuum" domain and require radically different mathematical techniques, such as direct simulation Monte Carlo (DSMC) and molecular dynamics methods to compute aerodynamics and heat transfer. From the standpoint of surface heat transfer, this regime is of little interest to the designer and will not be dealt with further in this review.

Further descent (with attendent reduction in flight velocity) brings the RV into the so-called "continuum" flight regime where increasing compressive and frictional forces cause a bow shock wave (a standing or stationary pressure wave) to envelop the vehicle. At the top of this continuum region is located what is termed the viscous or merged shock layer domain. This terminology refers to a state whereby the flowfield between the body surface and bow shock experiences a continuous set of velocity, temperature and species concentration profiles. The shock layer is in effect a very thick boundary layer terminating at the bow shock. Once inside this flight regime, the full suite of Navier-Stokes, energy and species governing equations can be applied. The viscous layer regime is the area where the well known "viscous shock layer (VSL)" subset of the N-S equations is applied. These approximation equations are discussed below. Continuing with the re-entry, at lower altitudes the Reynolds number increases dramatically (along with an associateds rapid fall in Knudsen number) and the shock layer flow separates into a thinner viscous layer underlying a semi-inviscid region with a high degree of vorticity.

Finally at the highest Reynolds numbers, the external flowfield separates into the well known inviscid/boundary layer flow. Returning to Fig. 2, the region of the plot delineated for radiation coupling at the highest entry velocities and dynamic pressures corresponds to an important flight regime encountered (as discussed above) for high speed Earth entry and outer planet entry missions. At the lower end of this region, incident surface sensible heat fluxes are high enough to induce pyrolytic breakdown of most thermal protection system (TPS) materials followed, in most cases, by vaporization (thermochemical ablation) of the material surface. This process injects significant amounts of mass into the shock layer, and in the process, absorbs large amounts of energy to protect the vehicle, but also is self correcting by directly convecting energy downstream. Unfortunately as the flight velocity increases, shock layer exitation with associated production of gas cap radiation directly impinges on the TPS surface. This radiative heat flux directly determines the shock layer temperature distributions and rate of surface ablation. Ablative mass injection can act to absorb some of this incident radiation, but the effect is less than for convective blocking. This latter situation is termed the "radiation/ablation regime". In this case the dominant factor in the flowfield governing equations is the radiation source term, and this must be accurately modeled. The mathematical coupling of the fluid mechanics and radiation becomes paramount. In the discussion to follow, the various phenomenological modeling techniques as well as governing equations (including full CFD techniques) which apply to each of these regions will be outlined. Particular attention will be focused on the induced surface effects of catalytic recombination, ablation and pyrolysis.

Governing Equations, Thermophysical Modeling and Mission Profiles

General

Each of the above described flight regimes and their related chemistry and physics requires a different set of modeling equations. Many past and current flight missions have encountered some or all of the flowfield thermophysical phenomena typified by each of these flight regimes. The discussion below focuses on sub-categories of these, and reference to the important computational issues of the various re-entry mission profiles is made. First, however, a general starting point for the computational science is needed. In any 3-dimensional reference frame, the invariant-vector representation of the Navier-Stokes equations, the constituent species conservation and total energy conservation equations take on the following forms.

Total Mass Conservation

$$\frac{\partial \rho}{\partial \tau} + \nabla \cdot (\rho \underline{V}) = 0 \qquad (1)$$

Species,α, Conservation:

$$\frac{\partial \rho_\alpha}{\partial \tau} + \nabla \cdot (\rho_\alpha \underline{V}) = \nabla \cdot (\rho \mathcal{D}_\alpha \nabla x_\alpha) + \mathcal{R}_\alpha \qquad (2)$$

Navier-Stokes Momentum Conservation:

$$\frac{\partial \underline{V}}{\partial \tau} + (\underline{V} \cdot \nabla)\underline{V} = -\frac{1}{\rho}\nabla P + \frac{\underline{F}}{\rho} + \frac{1}{\rho}\nabla \cdot \underline{\underline{\tau}} \qquad (3)$$

Total Energy Conservation:

$$\rho \frac{\partial H_T}{\partial \tau} + \rho(\underline{V} \cdot \nabla) H_T = \frac{\partial P}{\partial \tau} - \nabla \cdot \underline{q} + \nabla \cdot (\underline{\underline{\tau}} \cdot \underline{V}) + \underline{F} \cdot \underline{V} + W \qquad (4)$$

These equations represent and encompass any and all of the fluid physics, chemistry and radiation transport phenomena that can occur in continuum flight regime of interest for hypervelocity flight. Their solution in any particular flight case or entry mission requires an appropriate set of initial and boundary conditions to form a well posed problem. In hypersonic flight the following conditions are required for any flight domain.

1) Freestream conditions: Thermodynamic state variables (temperature, pressure, composition,e.g.)and velocity.

2) In-flow and Out-flow conditions: characteristic velocity, pressures constraints, Extrapolation of flow conditions.(Also, surface hydrodynamic conditions such as, slip, no slip or tangency would be included.)

3) Surface boundary conditions: von Neumann or Dirichlet conditions; i.e. surface heat flux and mass flux (either specified or via instantaneous surface mass and energy balance), specified surface concentration and temperature.

Although conditions 1) and 2) are somewhat obvious and, in most cases, are imbedded in the N-S solution algorithm, the surface boundary condition 3) invokes a full range of surface hydrodynamic, surface chemistry and thermophysical phenomena which need further elucidation. As outlined in Ref.8, these are generally expressible as;

Species, α, Surface Mass Conservation:

$$(\rho_\alpha \underline{v})_g + \underline{J}^g_\alpha = (\rho_\alpha \underline{v})_s + \underline{J}^s_\alpha + (\underline{R}_\alpha + \underline{S}_\alpha)(1-\epsilon_s) \quad (5)$$

where
$\underline{R}_\alpha$ = the mass rate of production of species α by heterogeneous (surface)reactions,
$\underline{S}_\alpha$ = the mass rate of injection (thermochemical ablation) of species α via surface vaporization and in-depth pyrolysis,
and,
ϵ_s = the volumetric porosity of the solid surface material (TPS).

Surface Momentum Conservation:

$$P_s = P_g + [(\rho \underline{v})_g + \frac{4}{3}\kappa\mu_{ave}\hat{s}] \cdot (\underline{v}_g - \underline{v}_s) + \frac{4}{3}(\mu \nabla \cdot \underline{v})|_g - \frac{4}{3}(\mu \nabla \cdot \underline{v})|_s . \quad (6)$$

Once having established the surface mass and momentum conditions, the total surface energy conservation can be written down.

Total Surface Energy Conservation:

$$(h_1 h_3)[-k_T \nabla T|_g - \sum_\alpha h_\alpha \underline{J}^g_\alpha + \underline{q}_R|_{net}] = \sum_\alpha h_\alpha (\rho_\alpha \underline{v}|_g - \rho_\alpha \underline{v}|_s) - (h_1 h_3) k_T \nabla T|_s \quad (7)$$

Equations (1)-(7), although completely general, are extremely compact and contain a multitude of information. To further understand the behavior of this equation set, specific subsets representing the three separate hypervelocity flight regimes discussed above are delineated. The governing equations for the Viscous Shock Layer, High Reynolds Number (Boundary Layer) and the Coupled Radiation/Ablation flow regimes are discussed in the following sections.

Viscous Shock Layer Region:

To properly represent the viscous shock layer behavior the N-S equations need to be written down in a form general enough to include the bow shock behavior, the full range of viscous effects in a viscous shock layer and be constrained by an appropriate set of boundary conditions appropriate for this flight regime. For this case (and all of the subsequent cases and discussion) the N-S set will be written in a specific body oriented, 3-D, coordinate system typically used in most CFD and other solution algorithms. Also, these equations will be simplified to an appropriate level accurate enough to describe most mass, momentum and heat transfer phenomena encountered and still eliminate extraneous details of complex 3-D flowfields. These simplifications result in the so-called "thin layer Navier- Stokes" equations which basically eliminate the cross-flow derivative terms. These terms are only necessary when such details of vortical flow, unsteady vortices and detailed wake flows are to be studied accurately. Most problems involving surface heating and TPS design for hypervelocity flight are computationally intensive enough that the numerical grid densities cannot be high enough to justify inclusion of the cross-derivatives in any case. Thus the Thin Layer Navier-Stokes equations are written as;

Total Continuity:

$$(h_1 h_3)\frac{\partial \rho}{\partial \tau} + \frac{\partial}{\partial s}(h_3 \rho u) + \frac{\partial}{\partial n}(h_1 h_3 \rho v) + \frac{\partial}{\partial t}(h_1 \rho w) = 0 \quad (8)$$

Species,α,Continuity:

$$(h_1 h_3)\frac{\partial \rho_\alpha}{\partial \tau} + \frac{\partial}{\partial s}(h_3 \rho_\alpha u) + \frac{\partial}{\partial n}(h_1 h_3 \rho_\alpha v) + \frac{\partial}{\partial t}(h_1 \rho_\alpha w) = \frac{h_3}{h_1}\frac{\partial}{\partial s}(\rho \mathcal{D}_\alpha \frac{\partial x_\alpha}{\partial s}) + h_1 h_3 \frac{\partial}{\partial n}(\rho \mathcal{D}_\alpha \frac{\partial x_\alpha}{\partial n}) + \frac{h_3}{h_1}\frac{\partial}{\partial t}(\rho \mathcal{D}_\alpha \frac{\partial x_\alpha}{\partial t}) + \mathcal{R}_\alpha \quad (9)$$

s-Momentum:

$$(h_1h_3)\frac{\partial \rho u}{\partial \tau}+\frac{\partial}{\partial s}(h_3\rho u^2)+\frac{\partial}{\partial n}(h_1h_3\rho uv)+\frac{\partial}{\partial t}(h_1\rho uw)+ h_3\rho uv\frac{\partial h_1}{\partial n}+\rho uw\frac{\partial h_1}{\partial t}-\rho w^2\frac{\partial h_3}{\partial s}=-h_3\frac{\partial P}{\partial s}+ \frac{4}{3}\frac{h_3}{h_1}\frac{\partial}{\partial s}(\mu\frac{\partial u}{\partial s})+h_1h_3\frac{\partial}{\partial n}(\mu\frac{\partial u}{\partial n})+\frac{h_1}{h_3}\frac{\partial}{\partial t}(\mu\frac{\partial u}{\partial t}) \quad (10)$$

n-Momentum:

$$(h_1h_3)\frac{\partial \rho v}{\partial \tau}+\frac{\partial}{\partial s}(h_3\rho uv)+\frac{\partial}{\partial n}(h_1h_3\rho v^2)+\frac{\partial}{\partial t}(h_1\rho wv) -h_3\rho u^2\frac{\partial h_1}{\partial n}-\rho w^2\frac{\partial h_3}{\partial n}=-h_1h_3\frac{\partial P}{\partial n} +\frac{h_3}{h_1}\frac{\partial}{\partial s}(\mu\frac{\partial v}{\partial s})+\frac{4}{3}h_1h_3\frac{\partial}{\partial n}(\mu\frac{\partial v}{\partial n})+\frac{h_1}{h_3}\frac{\partial}{\partial t}(\mu\frac{\partial v}{\partial t}) \quad (11)$$

t-Momentum:

$$(h_1h_3)\frac{\partial \rho w}{\partial \tau}+\frac{\partial}{\partial s}(h_3\rho uw)+\frac{\partial}{\partial n}(h_1h_3\rho vw)+\frac{\partial}{\partial t}(h_1\rho w^2) +\rho uw\frac{\partial h_3}{\partial s}+\rho vwh_1\frac{\partial h_3}{\partial n}-\rho u^2\frac{\partial h_1}{\partial t}=-h_1\frac{\partial P}{\partial t}+ \frac{h_3}{h_1}\frac{\partial}{\partial s}(\mu\frac{\partial w}{\partial s})+h_1h_3\frac{\partial}{\partial n}(\mu\frac{\partial w}{\partial n})+\frac{4}{3}\frac{h_1}{h_3}\frac{\partial}{\partial t}(\mu\frac{\partial w}{\partial t}) \quad (12)$$

Total Energy (Enthalpy) Conservation:

$$(h_1h_3)\beta_H\frac{\partial \rho H_T}{\partial \tau}+\frac{\partial}{\partial s}(h_3\rho uH_T)+\frac{\partial}{\partial n}(h_1h_3\rho vH_T)+ \frac{\partial}{\partial t}(h_1\rho wH_T)=\frac{h_3}{h_1}[\frac{\partial}{\partial s}(Pr\frac{\partial(\rho H_T)}{\partial s}+q_s^R) +\mu(\frac{4}{3}u\frac{\partial u}{\partial s}+v\frac{\partial v}{\partial s}+w\frac{\partial w}{\partial s})]+h_1h_3[\frac{\partial}{\partial n}(Pr\frac{\partial(\rho H_T)}{\partial n} +q_n^R)+\mu(u\frac{\partial u}{\partial n}+\frac{4}{3}v\frac{\partial v}{\partial n}+w\frac{\partial w}{\partial n})] +\frac{h_1}{h_3}[\frac{\partial}{\partial t}(Pr\frac{\partial(\rho H_T)}{\partial t}+q_t^R) +\mu(u\frac{\partial u}{\partial t}+\frac{4}{3}v\frac{\partial v}{\partial t}+\frac{4}{3}w\frac{\partial w}{\partial t})] \quad (13)$$

where,

$$\beta_H=1-(\frac{H_T}{RT}+\rho\frac{\partial h}{\partial P})^{-1}. \quad (14)$$

In the reduction process from equations (1) - (4) to the above, not only have cross derivatives associated with viscous effects been eliminated, but also those second order terms involving derivatives of metrics (i.e. h_1, h_2 and h_3) have been dropped for both clarity and because such higher order geometric effects are inconsequential for most hypervelocity flight bodies of interest. Consistent with these reduced equations the surface boundary conditions (equations (5) - (7)) can be written in terms appropriate to a body fixed coordinate system. namely;

Species, α, Surface Mass Conservation:

$$(\rho_\alpha v)_g+J^g_{\alpha,n}=(\rho_\alpha v)_s+J^s_{\alpha,n}+(R^n_\alpha+S^n_\alpha)(1-\epsilon_s) \quad (15)$$

Surface Momentum Conservation:

$$P_s=P_g \quad (16)$$

and,

Total Surface Energy Conservation:

$$(h_1h_3)[-k_T\frac{\partial T}{\partial n}|_g-\sum_\alpha h_\alpha J^g_{\alpha,n}+q_n^R|_{net}]= \sum_\alpha h_\alpha(\rho_\alpha v|_g-\rho_\alpha v|_s)-(h_1h_3)k_T\frac{\partial T}{\partial n}|_s. \quad (17)$$

Vehicle surface metrics have been defined as,

$$h_1=\sqrt{(\frac{\partial x}{\partial s})^2+(\frac{\partial y}{\partial s})^2+(\frac{\partial z}{\partial s})^2} \quad (18)$$

$$h_2=1 \quad (19)$$

$$h_3=\sqrt{(\frac{\partial x}{\partial t})^2+(\frac{\partial y}{\partial t})^2+(\frac{\partial z}{\partial t})^2}\ . \quad (20)$$

The above set of thin-layer Navier-Stokes equations is general enough to apply to any of the continuum flight regimes, including the viscous shock case being considered in this section. As a general 3-D set they can be solved along any entry trajectory (continuum) from the entry interface to the ground using modern CFD numerical techniques. Discussion of these methods and associated issues is deferred to the following section on high Reynolds number flow, since that region is the most widely studied area from the standpoint of TPS design. However, there is a class of re-entry problems for which the specific aspects of merged and viscous shock behavior is important. For mission profiles which require a spacecraft to return from high Earth orbit, e.g. geosynchronous orbit (GEO) to low Earth orbit (LEO), the entry problem usually consists of the use of an aerobraking pass followed by return to LEO. These missions are relegated to higher altitude perigees, during which a significant portion of the flight will be in the viscous shock region. Depending on the vehicle ballistic coefficient and entry velocity, such missions may experience high Reynolds number flow (e.g. boundary layer flow) during the peak heating portion of the flight. In spite of this, solution techniques which depend on the lower Reynolds number for a viscous shock flow have been succesfully applied to these problems. To date these solution methods have been restricted to the 2-D axisymetric limit of the governing equations, either by the nature of the vehicle geometry and zero angle-of-attack mission profile or by virtue of a lack of interest in investing further computational resources for this problem. The 2-D axisymmetric set of equations is a subset of equations (8)- (17) whereby the vehicle/flow metrics take on the

following limits;

$$h_1 \longrightarrow 1 + \kappa y \tag{21}$$

$$h_2 = 1 \tag{22}$$

$$h_3 \longrightarrow r \tag{23}$$

Examples of the so-called "Viscous-Shock" or VSL methods come from the classic works of Davis[9], Miner and Lewis[10], Moss[11] and Gupta[12]. Briefly, without a long discourse on the method, the general VSL numerical algorithmic approach is to treat the above subset of 2-D axisymmetric N-S equations, in the steady state limit, as a parabolic set of partial differential equations, with known conditions at the origin of the computational domain. By providing an estimate of the funtional form of the surface pressure distribution along the body at, and in the vicinity of the stagnation point, the N-S equations and associated species mass and total energy conservation equations can be numerically differenced and solved via an appropriate downstream marching technique. In this process the complete shock-layer, including the bow shock can be numerically constructed and all field variables obtained throughout the computational domain. For more in-depth study and details, the reader is referred to the above references. The VSL methodology has been applied to several actual NASA flight missions and proposed flight experiments. A few example results will be discussed next.

Shown in Fig. 3 (Ref. 14) is a sketch of the flight geometry and flowfield of a previously proposed major NASA flight test mission known as AFE. This flight was planned to perform an aerobraking pass from LEO (launch from orbit by shuttle orbiter) to LEO under the impetus of a solid rocket. The altitude vs. time history of the flight is plotted in Fig. 4. Figure 5 provides a plot of Reynolds number (behind a normal shock and based on body diameter) as a function of time for this trajectory and shows that the primary period of peak heating will be in the full continuum regime. However, significant portions of the flight are in the VSL region. Various computational methods have been applied to this flight, including full N-S, VSL and boundary layer techniques. Stewart, etal[14] have presented a comparison of the pertinent heat transfer effects for AFE based on these three different techniques. These computations were performed with the following simplified subset of surface boundary conditions as stated in equations (15)-(17);

Species,α,Surface Mass Conservation:

$$J^g_{\alpha,n} = R^n_\alpha \tag{24}$$

Surface Momentum Conservation:

$$P_s = P_g \tag{25}$$

and,

Total Surface Energy Conservation:

$$-k_T \frac{\partial T}{\partial n}|_g - \sum_\alpha h_\alpha J^g_{\alpha,n} + q^R_n|_{net} = 0. \tag{26}$$

Surface heterogeneous reactions embodied in the terms, R^n_α, consist of the irreversible surface recombination reactions of nitrogen and oxygen (i.e. N + N = N_2 and O + O = O_2) using surface kinetics expressions emprically determined for Shuttle tiles with RCG (Reaction Cured Glass) coating. As shown in Figure 6, computed surface temperatures using the reacting, non-similar boundary layer code BLIMPK[15] have similar magnitudes and distributions when using non-equilibrium boundary layer edge conditions taken from full N-S (LAURA code) (Gnoffo[16]) and VSL (Gupta[12]) solutions for the AFE configuration. Obviously at altitudes of 75 km and above, the use of equilibrium boundary layer edge conditions will not give adequate results. Figure 7 shows a comparison of edge conditions taken from equilibrium, from non-equilibrium VSL and LAURA N-S solutons for AFE. There is a vast departure from equilibrium and even significant differences between N-S and VSL edge conditions at 75 km. These kinds of non-equilibrium effects are typical of shock-layer behavior in the viscous shock flow regime and indicate the necessity of accounting for this unique behavior in these higher altitude heat transfer computations.

Finally, the VSL technique has, in the past, been successfully applied to analysis of Shuttle Orbiter centerline heat transfer computations and compared with Orbiter flight data. Thompson[15] has performed VSL centerline hypersonic flow computations for the Orbiter at altitudes above 60 km. Figure 8 shows a comparison of Shuttle centerline heat transfer at 75 and 64 km (Mach 25 and Mach 18) using the same surface boundary (finite rate catalysis) conditions as in equations (24)-(26). To within the variation in surface catalysis models the agreement is excellent.

High Reynolds Number (Boundary Layer) Flow Regime

At lower altitudes for re-entry trajectories (e.g. less than 65 km in air), most RV's will experience peak heating under conditions of high Reynolds number flow where the shock layer separates into a well defined inviscid outer layer and a contiguous, near surface boundary layer. Since this is a most important flow regime from the standpoint of aerothermodynamics and TPS design, some discussion will be focused on the applicable state-of-the-art Navier-Stokes solution techniques. Certainly the traditional two-layer inviscid/ boundary layer techniques, and even Fay and Riddell stagnation heat transfer simplified relations can be used here for engineering level heat transfer estimates using simplified geometry assumptions. (i.e. axisymmetric flow, tangent

cone, tangent wedge and flat plate approximation methods, cf. Ref. 16). However, in this paper the focus will be on the more recent applications of 2-D and 3-D CFD Navier-Stokes solution techniques with some examples of applications.

Equations (8)-(14) along with surface boundary conditions (15)-(17), the necessary gas phase reaction rate kinetics, and thermal and caloric equations of state comprise the complete set of real gas governing equations which most current CFD N-S solvers address. If the reentry velocity is high enough then this equation set must be supplemented with transport relations for shock layer gas spectral radiative fluxes and TPS material and surface ablation thermophysical models. These latter effects will be the subject of the next section. Although there are many different and varied numerical techniques currently being used to solve these N-S equations for real gas flows (including algorithms for massively parallel processors), the author is most familiar with three algorithms which have been most widely applied to problems within NASA, and this discussion will be limited to this group. For 2-D axisymmetric problems, without coupled radiation heat transfer, the fully implicit Gauss-Seidel method of Candler and MacCormack[17] has found wide application to real gas, high Reynolds number flows. As with other CFD numerical N-S solvers, this method is based on the time-hyperbolic nature of the N-S set. Hypersonic flowfields are comprised of mixed sub-sonic and supersonic domains, the mathematical characteristics of which are different. Fully steady state sub-sonic domains possess characteristics of elliptic PDE's, while the supersonic domains are hyperbolic. Numerical techniques which can handle both computational domains within the same problem are very cumbersome and can be ill-behaved (i.e. difficult to converge and unstable). If the time derivative terms are retained, then the entire computational domain is hyperbolic in time and time accurate and pseudo-time accurate time marching algorithms can be applied. This mathematical feature is universal in current CFD N-S Solvers. The Gauss-Seidel implicit method is based on a spatial discretezation of the governing equations using upwind biased, modified Steger-Warming flux functions (or flux splitting method). All terms are forward differenced in time to result in a fully implicit, time updated scheme. The set of resulting matrix, difference equations is solved at each time update across the computational domain via the line-by-line Gauss-Seidel direct matrix inversion scheme. This method is extremely efficient computationally because of the relatively non-sparse matrices which are generated. Courant-Friederichs-Lewy numbers (CFL) as high as 500 have been routinely achieved with this method. However, its drawback is that, with modern supercomputers (at least using a single processor), memory restrictions will, practically speaking, only permit its application to 2-D axisymmetric problems. Three-D problems will generate extremely large matrices, particularly for problems involving even a modest number of chemical species and reactions. For 2-D axisymmetric problems, the Gauss-Seidel N-S solver technique has been successfully applied to a number of NASA mission scenarios. Among these is the Mars Pathfinder entry vehicle that landed on Mars on July 4,1997. This set of computations involves coupled ablation from the heat shield and will be discussed in the next Section. However, an example of a non-ablating system is given in Fig. 9 (Ref. 13) and shows the computed behavior for the temperature excursion expected in the previously proposed AFE wall catalysis experiment. A specific ceramic tile located near the flowfield centerline is coated with a highly reactive (or catalytic) catalytic overcoat. As shown in the plot a temperature increase of at least 150 K can be expected. This result was obtained using a 2-D axisymmetric shape approximation for the AFE flowfield and the Gauss-Seidel algorithm was employed with the reacting wall boundary conditions of equations (24)-(26). The solution was obtained at the expected peak heating point for AFE.

A second widely employed 3-D CFD real gas method is the point-implicit, TVD (Total Variation Diminishing) algorithm, most successfully embodied in the Langley Research Center LAURA code by Gnoffo[18]. The LAURA code employs a numerical scheme originally developed by Coakley[19] which employs upwind biased spatial differencing for a given set of cell face flux functions. Forward (implicit) time differencing is invoked on a point-by-point basis in the domain. This technique generates a series of compact matrix equations for the cell averaged field variables for each sweep through the computational domain. When employed with a selected residual or solution variation reduction scheme, this results in very efficient solution iteration. However, the limited degree of implicitization limits the advancement of CFL numbers in the range of one (1) to five (5). Readers are very much encouraged to consult Ref. 18 for more numerical details. The LAURA code currently employs Roe flux difference splitting for flux function evaluation. Cell average solution variables can be reconstructed to cell faces with accuracies of up to one and one half (1.5) orders. The code is a complete reacting, real gas, N-S solver and includes air and Mars atmosphere gas reaction kinetics. Finite rate surface catalysis boundary conditions and a modified Baldwin-Lomax algebraic turbulence model are installed. The code can be run with finite volume grids subdivided into multiple grid blocks and a form of grid mesh density sequencing can be accomplished. For problems requiring a very large number of grid points (e.g. the complete flowfield of the Shuttle Orbiter) supercomputer memory limitations will require the multi-block approach with LAURA. Solutions are obtained for individual sub-blocks and then reconstructed to yield the full domain solution. An example of the application of LAURA and of the use of the multi-block approach is given by Weilmuenster,et al[20] and Gnoffo,et al[21]. These two studies have pro-

vided detailed LAURA results for both aerodynamics and aerothermodynamic heating of the Shuttle Orbiter at selected critical points along the Orbiter re-entry trajectory. Figure 10 (Ref. 20) shows a schematic of the general grid layout for these Orbiter computations and is fairly typical of a LAURA finite volume grid. Using the multiblock approach mentioned above, the results from Gnoffo's[21] study can be typified by the normalized heat transfer distribution plots shown in Figs. 11 -14. Figure 11 shows the heating distribution along the windward centerline along with comparisons with alternate engineering techniques and with flight data. As is typical with most 3-D CFD results, agreement with flight is excellent for this portion of the flowfield. A similar plot is provided in Fig. 12 for the leeward centerline heating, and, where flight data is available, agreement is either adequate (where heating is low) or quite poor. These discrepancies are usually due to inadequate grid resolution in regions of rapidly accelarating or deccelarating flow (or for shock-shock interactions). The remaining plots (Figs. 13 -14) show the off-centerline predictive capability of LAURA, and the results are generally quite good. These computations were performed using a seven species gas reaction kinetics model, temperature dependent transport properties and a two-temperature nonequilibrium thermal model.

A final example of high Reynolds number real gas flow computations with surface catalysis is discussed here from the standpoint of a slightly different computational approach for the 3-D CFD algorithm. Recently NASA has embarked on a series of studies and flight test programs (e.g. X33 and X34) to develop reusable launch systems to drastically reduce the cost of payload insertion into LEO. A NASA Access-to-Space study[22] presented several alernate launch system scenarios, including an airbreathing NASP single-stage-to-orbit (SSTO) option, a hybrid airbreathing/rocket two-stage-to-orbit (TSTO) case as well as a separate single-stage-to-orbit pure rocket (SSTOR) configuration. Weight statements, required technologies, fixed and variable costs and space launch infrastructure impacts of each of option were reported. It is well known by now that the SSTOR option was selected, and is being pursued in the form of the X33 flight test vehicle program. As a part of the NASA reusable launch vehicle (RLV) technology development program which followed the Access-to-Space Report, NASA Ames Research Center developed a more systematic approach to the design process for TPS selection and sizing. The method involves solving the 3-D real gas CFD flowfield solutions to obtain detailed surface heat transfer rates for the actual SSTOR vehicle configuration at selected "anchor points" along the TPS design limiting trajectory. These heating environments are then interpolated in time along the trajectory, thus forming an input database for time dependent in-depth conduction and TPS sizing computations for each surface body location. In this manner a detailed 3-D surface material and thickness map can be obtained, and more accurate estimates of TPS mass distributions can be realized. An example of the CFD heat transfer results obtained in this study is given in this discussion. A more detailed accounting is provided in the last Section of this paper. TPS heating environments have been obtained for a generic winged-body SSTO rocket configuration developed by the Langley Research Center (LaRC). A computational surface grid which defines the geometric configuration is depicted in Fig. 15. Henline,et al[23] have employed the numerical methods an real gas modeling contained in the GASP (version 2.2) CFD N-S solver to compute the heating environments on this vehicle.

The GASP code, developed by Aerosoft, Inc.[24], is a general purpose, finite volume based, 3-D real gas Navier-Stokes solver. It contains a variety of gas phase chemical kinetics, thermal and thermodynamic and transport property models. These include models for air, $H_2 - He$ and (at Ames Research Center) CO_2 atmospheres. The code is unique in that a variety of finite volume, spatial differencing schemes can be applied to a given problem through the use of optionally available flux functions. These include full flux, Steger Warming, Van Leer, Roe and Roe/Harten flux and flux diference split functions. If the user determines that the individual characteristics of each of these flux functions has a unique advantage in any particular coordinate direction, then that flux splitting method can be so applied. GASP 2.2 uses first, second or third order MUSCL variable reconstruction stencils based on user choice. In addition to the above features, GASP employs a variety of time integration strategies which can be used according to the nature of the problem. These schemes can be used to perform time integration in either a global or space marching manner (if flow characteristics warrant it). These include 3-factor AF (approximate factorization), 2-factor AF with line relaxation, LU-decomposition-for 2-D space marching and m-stage Runge-Kutta time accurate methods. Finite volume computational grids can be constructed in a zonal manner so that different time integration strategies can be used in each zone where appropriate. Convergence acceleration schemes such as mesh sequencing, CFL ramping and (in more recent version) multi-grid techniques can be used. In all of the implicit schemes used for GASP, the full implicit matrix is not used, but only approximations of the inverse are applied to the right-hand side of the matrix equations (e.g. 3-factor and 2-factor AF). Because of this, the ultimate upper limit of possible CFL numbers for any given problem is somewhat restricted. In large 3-D reacting flow hypersonic problems, the author has experienced CFL values limited to the range of 5 to 10. Finally, the GASP code architecture has been designed to be very memory efficient and can be run in both plane and zonal parallel modes on multi-processor Cray machines.

As discussed in Ref. 23, for the LaRC SSTOR Access-to-Space vehicle shown in Fig. 15, the GASP (Version

2.2) code has been used to perform full 3-D flowfield reacting, real gas aerothermodynamic heating computations at several points along the TPS design limiting entry trajectory for this configuration. These have been performed using a 5-species air gas kinetics model, single temperature thermal model, constant Schmidt number based mass diffusion coefficients and temperature dependent thermal conductivity and viscosities. Both laminar and Baldwin-Lomax algebraic turbulence model results have been obtained using finite rate surface catalysis and surface radiative equilibrium boundary conditions. The surface boundary conditions have been implemented for a variety of possible TPS material mappings. Solutions have been obtained using the full Navier-Stokes set of momentum equations with van Leer inviscid flux functions. First order differencing was found to be adequate in the streamwise and circumferential directions, while is was necessary to resort to third order reconstruction in the normal direction to obtain accurate estimates of surface heat transfer. The 2-factor AF algorithm with streamwise relaxation was used for time integration. The maximum CFL number reached for these cases was five (5). Approximately 30 hrs. of Cray C-90 CPU time was required to converge a solution to $4\frac{1}{2}$ levels of L2-Norm residual reduction for a grid density of approximately 400,000 nodes. All of this was accomplished with less than 18 megawords of Cray run time memory.

Typical results from these simulations are presented in the folowing sequence of figures. Figure 16 shows the full 3-D finite volume flow grid at a sequence level of 161 X 65 X 38 cells. In such cases, usually at least three grid sequence levels are employed. In the case studied here, two levels of grid density were used for the streamwise and normal coordinate directions and found to be sufficient for grid independence. Figure 17 depicts the TPS material mapping used for this vehicle, which is in accordance with that proposed in the Access-to-Space Study Report[22]. RCG coated Carbon-Carbon or TUFI tiles (Toughened Unipiece Insulation) are used for higher temperature regions (nosecap and leading edges) while TABI (Tailorable Advanced Blanket Insulation) and AFRSI (Alumina Flexible Reusable Surface Insulation) blankets are used elsewhere. Surface kinetics for oxygen and nitrogen recombination reactions on each of these materials were obtained from Stewart, etal[25]. The resultant GASP computational results for the radiative equilibrium surface temperature are shown in Fig. 18 for fully laminar flow and in Fig. 19 for turbulent flow. These simulations were performed near the peak heat transfer rate portion of the LaRC SSTOR trajectory (1300 sec from entry interface, at 58 km altitude and 32° angle-of-attack). Although it is hard to see in the grayscale plots, near the division between the Carbon-Carbon (C-C) nosecap and the windward TABI blankets, there is a substantial jump in temperature due to the highly catalytic nature of TABI in comparison to the C-C. Finally, in Fig. 20 a larger scale view of the wing/winglet region is shown to detail the effect of impingement of the bow shock wave on the leading edge surface. The shock-shock interaction results in the highest temperatures on the vehicle, reaching nearly 2000 K.

The Coupled Radiation and Ablation Flow Regime

In Fig. 2 the region in the lower right portion of the plot at the highest velocities and lowest altitudes corresponds the the flight regime where the kinetic energy levels are high enough, that when dissipated via a shock layer will exite the radiation exchange mechanisms in the gas to high enough rates to produce substantial gas cap radiation fluxes. In this flight regime these radiative fluxes will be high enough to penetrate the optical interference (absorption) of the shock layer gases and impinge directly on the TPS. This will begin to happen in air (Fig. 2) at velocities above (25,000 ft/sec) 8 km/sec. For almost all mission scenarios, entries into the Venusian atmosphere and into Jupiter or Saturn will result in flow regimes in this so-call "radiation/ablation coupled" domain. The term "radiation coupled" or "radiation dominated" is used to refer to dominance of the gas phase radiative flux terms appearing in the total energy (enthalpy) conservation equation(Eq. (13)). When this term is the overwhelming factor in the shock layer energy balance, both enthalpy (temperature), species concentration and velocity profiles will be fully governed by the radiation processes. Obviously, accurate determination of the radiation flux terms in analytical forms compatible with Eq. (13) is a critical factor when attempting to compute both the flowfield and surface heat fluxes on vehicles operating at these high energies.

When solving the governing equations for these cases, in principle the complete set of terms in equations (8)-(14) and boundary conditions (15)-(17) are required. Since the extremely high incident radiative heat flux at the surface will inevitably cause massive TPS ablation which injects mass into the shock layer at high rates, significant additional coupling of this ablation hydrodynamics and the external flowfield will occur. This fact will have a significant impact on the mathematical characteristics of the resultant shock layer flow. Figure 21 is a sketch of this general type of behavior for such a massive ablation condition. Ablation species exit the wall at high enough velocities so that a blowing sub-layer which has nearly inviscid flow properties, forms near the wall. The thickness of this layer depends on the blowing rate. The sub-layer flow then intercepts the incoming inviscid flow from the bow shock, forming a viscous mixing layer at the intersection. The various different material layers present in the ablative TPS are also shown in Fig. 21. Also shown are representations of the general behavior of the radiation processes in the different shock layer flow regions. Emission is dominant in the usually optically thin inviscid layer, while the denser (cooler) layer of ablation products will cause absorption to dominate near

the wall. As a consequence of these very large coupling effects any numerical N-S solution technique will have to be quite different and more robust than those currently in use for non-ablating situations. For this reason, there are currently no fully developed 2-D or 3-D Navier-Stokes solution techniques which completely include all of the radiation and ablation (mass injection) effects for coupled radiation/ablation problems. There are two extremely difficult issues needing resolution to allow such a fully coupled algorithm. The first is centered around the inclusion of very high mass injection rates into the surface mass and energy balance boundary conditions. These high rates will, in any time accurate or pseudo time accurate transient solution method, result in very massive (almost discontinuous) surface cell updates, which in turn will cause massive instabilities unless handled by some type of implicit formulation. This means that the full set of ablation/ radiation boundary conditions must be incorporated into the numerical Jacobians of the difference equations. For any real gas problem with a large number of species and radiation, this is an algebraically daunting task and has not yet been done and is certainly a subject of future research.

The second difficult numerical issue is the coupling of the radiation source terms, q_s^R, q_n^R and q_t^R. Computation of the individual radiative flux terms at any given point in the flowfield requires an integration over all of the radiative, species and temperature profiles throughout the entire computational domain. This must be repeated for each numerical computational point in the flowfield. Such an elliptic problem is currently beyond the capabilities of today's most powerful supercomputers. Approximations must, have been and will be made to simplify this situation. The remaining portion of this section is thus devoted to a brief description of the current simplified techniques for solving this coupled radiation/massive ablation problem. Some examples of past design results will be given.

Prior to this, however, an example of a partial exception to the above conclusion will be discussed. In a case where there is minimal radiation and incident convective heat fluxes are high enough to cause only modest ablation and mass injection, it has been possible to obtain CFD solutions with coupled ablation. This has been done in the design phase of the recent NASA Mars Pathfinder mission entry probe forebody heat shield. Chen, etal[26] has used the 2-D axisymmetric Gauss-Seidel algorithm to perform full Navier-Stokes solutions at selected points along the design entry trajectory for Mars Pathfinder. These solutions (for the predominantly CO_2 Mars atmosphere) were loosely coupled to time dependent, in-depth conduction/pyrolysis/ablation solutions for the surface blowing rates, surface temperatures and in-depth TPS temperatures of the Pathfinder SLA-561V heat shield ablative material. Several iterations, at each trajectory point, between the CFD N-S solver and the in-depth conduction code were required to converge on resultant matching surface temperatures, blowing rates and heat fluxes. Figures 22 and 23 show the surface heat flux distributions and components for this 70-deg. sphere-cone shaped flight body.Figures 24 and 25 give the results for in-depth TPS material temperatures at the stagnation point and one downstream location. To the author's knowledge, this is the only fully coupled CFD/ablation solution thus far obtained.

In the past, fully coupled radiation/ablation solutions have been limited to 2-D axisymmetric configurations with severe restrictions on the fidelity of the flowfield modeling. Solutions have been based exclusively on steady state, algebraic algorithms. The governing set of equations (which are a subset of equations (8)-(14)) have, in most situations, taken the following forms.

Total Continuity:

$$\frac{\partial}{\partial s}(h_3\rho u) + \frac{\partial}{\partial n}(h_1 h_3 \rho v) = 0 \tag{27}$$

Species,α,Continuity:

$$\frac{\partial}{\partial s}(h_3\rho_\alpha u) + \frac{\partial}{\partial n}(h_1 h_3 \rho_\alpha v) = h_1 h_3 \frac{\partial}{\partial n}(\rho \mathcal{D}_\alpha \frac{\partial x_\alpha}{\partial n}) \tag{28}$$

s-Momentum:

$$\frac{\partial}{\partial s}(h_3\rho u^2) + \frac{\partial}{\partial n}(h_1 h_3 \rho u v) = -h_3\frac{\partial P}{\partial s} + h_1 h_3 \frac{\partial}{\partial n}(\mu \frac{\partial u}{\partial n}) \tag{29}$$

Total Energy (Enthalpy) Conservation:

$$\frac{\partial}{\partial s}(h_3\rho u H_T) + \frac{\partial}{\partial n}(h_1 h_3 \rho v H_T) = h_1 h_3[\frac{\partial}{\partial n}(Pr\frac{\partial(\rho H_T)}{\partial n} + q_n^R) + \mu(u\frac{\partial u}{\partial n} + \frac{4}{3}v\frac{\partial v}{\partial n} + w\frac{\partial w}{\partial n})], \tag{30}$$

with the following set of simplified surface boundary conditions.

Species α Surface Mass Conservation:

$$(\rho_\alpha v)_g + J_{\alpha,n}^g = (\rho_\alpha v)_s + S_\alpha^n(1-\epsilon_s) \tag{31}$$

and,

Total Surface Energy Conservation:

$$(h_1 h_3)[-k_T \frac{\partial T}{\partial n}|_g - \sum_\alpha h_\alpha J_{\alpha,n} + q_n^R|_{net}] = \sum_\alpha h_\alpha(\rho_\alpha v|_g - \rho_\alpha v|_s). \tag{32}$$

The in-depth solid (TPS) conduction terms have not been included, since these effects having been lumped

into an apriori empirical determination of the thermochemical ablation rate. This is usually done through the use of a correlation for the TPS material "effective heat of ablation". The algorithm most often used to solve this so-called "thin viscous shock" set of geoverning equations is that used in the RASLE[27] code used to design the Galileo probe forebody heat shield. This algorithm integrates the coupled equations by means of a parabolic marching technique reminiscent of integral boundary layer methods. It is an inverse, shock fitting technique in which the shock standoff distance and streamwise shape are estimated by a correlation developed by Falanga and Olstad[28]. The governing equations are discretized across the shock layer using polynomial expansions which encorporate a matching parameter to match expansions from the surface and shock boundaries at the inviscid/blowing layer interface. Radiative fluxes are computed using a "tangent slab" or plane-parallel approximation. In this model the radiation view factor in the shock layer is assumed to exist only along a line of sight normal to the body surface. It is a good approximation for thin shock layers and near stagnation streamlines. In all solutions to date, all radiation processes have been assumed to in equilibrium, i.e. whereby emission is equal to absorption at each point in the flow. Scattering and reflection have been neglected. A full suite of radiation exchange events and processes have been modelled. These include line radiation, molecular continuum radiation, as well as photo-ionization events. As outlined in Ref. 27, line radiation has been accounted for by using a lumped band approach, with up to twenty (20) bands possible in the RASLE code. Radiation property models have been developed for this method which can be applied to air, the Jovian atmosphere ($H_2 - He$) and the CO_2 system (Venusian atmosphere).

As a brief example of the types of solutions possible with an algorithm like RASLE, some results from the preliminary design of the proposed ESA/Rosetta Comet return mission probe will be given. Henline and Tauber[29] have used the RASLE methodology to compute net surface heat fluxes, surface temperatures and TPS surface ablation and recession rates by coupling the RASLE code to the in-depth conduction/pyrolysis/ablation code CMA[30] along the proposed ESA/Rosseta probe entry trajectory. Figure 26 shows a simple sketch of the probe's forebody geometry, while the entry trajectory is shown in Fig. 27. The probe returns to Earth with an entry speed of 16 km/sec resulting in very high radiative fluxes. As can be seen from Fig. 28, the stagnation point radiation pulse (accounting for ablation) peaks at 1.2 kw/cm^2, which is about 60% of the total. Figure 29 shows the surface heat flux and tempertures (from a coupled solution with CMA) along the entry trajectory. Substantial ablation rates occur for the carbon-phenolic heat shield material selected for this mission. These, along with the computed recession rates are shown in Figs. 30.

The NASA Galileo probe to Jupiter represents one of the most severe entry problems ever attempted and analyzed via the thin VSL/radiation/ablation techniques discussed above. This probe entered the Jovian atmosphere at a relative velocity of 48 km/sec. The resultant flowfield is radiation dominated and the probe was predicted to lose about 50% of its' carbon-phenolic heat shield mass in the first 10 sec of the heating pulse. The as designed probe is shown in Fig. 31 and the RASLE code computed peak radiative and convective surface heat fluxes are shown in Fig. 32. Approximately 95% of the net surface heat flux is incident radiation.

A Case Study in CFD Based TPS Design

During the technology development phase of the Access-to-Space reusable launch vehicle program in NASA, CFD based techniques were developed to make it possible to obtain a higher degree of accuracy or fidelity in the selection and thickness determination of TPS materials for RLV type vehicle concepts. The philosophy taken here was that with 3-D real gas Navier-Stokes solvers like GASP, there is enough computational efficiency to allow the determination of full 3-D body surface heat transfer distributions over any general 3-D RLV shape, and that this can be done at enough trajectory points to allow coupling of these surface heat transfer rates to a transient 1-D conduction TPS design code. As detailed in Ref. 23, this is in fact true.

A test design case was selected which focused on the TPS design for the LaRC winged-body SSTOR concept and its' associated entry trajectory. This configuration and some selected results for surface temperatures was discussed previously (see Figs. 18 and 19). The re-entry trajectory plot for this mission is given in Fig. 33. Shown here are discrete points which have been selected as so-called "CFD anchor points" to characterize the heating pulse experienced by the RLV. In Fig. 34, the rational for the selection of these point should be clear. It can be seen that each point anchors a given heating rate-time curve distinct feature. Between these features the heat transfer profile is relatively linear (or flat) and it is assumed that the full 3-D surface heat transfer rates obtained from CFD at these points can be linearly interpolated in time to provide an input database for a trajectory based transient conduction code. Figure 34 also shows the final CFD stagnation results for the anchor points. Although the magnitudes are different (as expected), the general shape of the distribution is similar to the initial engineering estimates. Using GASP (Version 2.2) winged-body RLV solutions were obtained with a specified TPS material mapping at each anchor point. Partial catalytic, radiative equilibrium surface boundary conditions were applied. From these solutions a database of recovery temperatures and associated heat transfer coefficients was constructed at each trajectory time point. These data were then used as input database for an implicit transient conduction code (OMLITS[23]) which sim-

ulated the surface energy balance and in-depth temperature profiles thru the proper TPS stack-up for each of 10,500 vehicle body points. By constraining the conduction code material interface and backface boundary conditions to the proper material maximum temperature limits, minimum TPS material thicknesses could be estimated for each RLV body point location. This result was achieved with only one iteration between the CFD trajectory solutions and the conduction solver. As reported in a study by Chen and Milos[31], even with very high in-depth conduction heat transfer rates, approximately converged flowfield/transient conduction solutions can be obtained to within 5% in a single iteration provided there is no ablation or mass injection. A conclusion such as this is a result of the relative insensitivity of surface heat and mass transfer coefficients to surface temperature. In principle the near surface hydrodynamic state and thermophysics determines these coefficients. The CFD solution determine the near surface hydrodynamics and thermophysics. Results of this design/sizing analysis for the LaRC RLV mission are given in Figs. 35 and 36. Figure 35 displays the full 3-D vehicle distribution of top layer TPS thicknesses, and Fig. 36 includes a centerline line plot of these values. Since, as part of the TPS material stack-up, lumped structural thickness were included, the effect of these structural "thermal masses" is quite evident in Fig. 36.

In closing, a brief reference is made here to the current application of this CFD/trajectory based TPS design to the now on-going NASA/Lockheed Martin X33 prototype flight test vehicle project. A full spectrum of GASP and LAURA 3-D real gas CFD solutions are being developed to construct a comprehensive aerothermodynamic database for TPS design. Figure 37 shows one GASP (Version 3) solution for the X33 configuration near the peak Mach 15 in its' design trajectory. This plot shows the general nature of the surface temperature distribution, and in addition, reveals important features of the external flowfield. In particular the effects of a shock-shock-surface impingement can be seen near the root of the canted fin. Solutions of this type to examine many TPS heating and design details are now continuing. The approach being taken in development of the X33 aerothermal design database has gravitated away from focus on given trajectories to that of performing CFD solutions at carefully selected design points which cover the entire possible flight envelope for the X33 mission. In this manner, a database (which can be accurately interpolated) can be developed independently of any specific trajectory. This permits TPS designs which can be rapidly revised during the vehicle design cycle. Thus a minimum number of somewhat expensive CFD solutions can be used for the entire design process. Figure 38 shows a plot of the current database space for X33 aerothermodynamic solutions which spans several design trajectories and a flight envelope which encompasses the proposed flight design space.

Summary and Conclusions

The above review of hypersonic re-entry flowfield analysis techniques when applied to problems with surface thermochemistry (e.g. surface catalysis), radiation and ablation indicates that, if the modern implicit and partially implicit 2-D and 3-D Navier-Stokes codes are properly utilized, then flowfield solutions, surface heat transfer, and TPS design can be performed at the final design level with CFD/trajectory based techniques. This conclusion is, however, restricted to the TPS design for missions which do not experience radiative heating and ablation coupling. Major research is needed to extend the methodology to this flight regime. As such, this design process is now being applied to the current NASA X33 and RLV flight projects. This has never been done before and represents a significant advancement in design tool development.

References

[1] Lees, L., "Laminar Heat Transfer Over Blunt Nosed Bodies at Hypersonic Speeds," *Jet Propulsion*,Vol. 26, No.4, pp. 259-269, 1956.

[2] Fay, J.A. and Riddell, F.R.,"Theory of Stagnation Point Heat Transfer in Dissociated Air," *Journal of the Aerospace Sciences*, Vol. 25,No. 2, pp. 54-67,1958.

[3] Kemp. N.H., Rose, P.H. and Detra, R.W.,"Laminar Heat Transfer Around Blunt Bodies in Dissociated Air," *Journal of the Aerospace Sciences*,pp. 421-430, July 1959.

[4] Goulard, R.,"On Catalytic Recombination Rates in Hypersonic Stagnation Heat Transfer," *Jet Propulsion*,Vol. 28, pp.737-745, November 1958.

[5] Howe, J.T.,"Hypervelocity Atmospheric Flight:Real Gas Flowfields," NASA TM 101055, June 1989.

[6] Probstein, R.F.,"Shock Wave and Flow Field Development in Hypersonic Reentry," *American Rocket Society Journal*,31,pp. 184-194, Feb. 1961.

[7] Edelman, R.K. and Fortune, D.,"Mixing and Combustion in the Exhaust Plumes of Rocket Engines Burning RP1 and Liquid Oxygen," TR-631 General Applied Science Laboratories, Inc., Nov. 1966.

[8] Engel,C.D.,"Ablation and Radiation Coupled Viscous Hypersonic Shock Layers," Volume I, Ph.D. Thesis, Dept. of Chem. Eng., Louisiana State University, Baton Rouge, La., NASA Grant NGR 19-001-059, Langley Research Center, October 1971.

[9] Davis, R.T.,"Numerical Solution of the Hypersonic Viscous Shock-Layer Equations," *AIAA Journal*,Vol. 8, No. 5, pp. 843-851, May 1970.

[10] Miner,E.W. and Lewis,C.H.,"Hpersonic Ionizing Air Viscous Shock-Layer Flows over Non-Analytic Blunt Bodies," NASA CR-2550, May 1975.

[11] Moss, J.N.,"Reacting Viscous-Shock-Layer Solutions with Multicomponent Diffusion and Mass Injection," NASA TR R-411, 1974. [12] Gupta, R.N. and Simmonds, A.L.,"Hypersonic Low-Density Solutions of the Navier-Stokes Equations with Chemical Nonequilibrium and

Multicomponent Surface Slip," AIAA Paper 86-1349, June 1986.

[13] Stewart, D.A. and Kolodziej, P.,"Wall Catalysis Experiment on AFE," AIAA 88-2674, AIAA Thermophysics, Plasma Dynamics and Lasers Conference, June 27-29,1988, San Antonio, TX.

[14] Stewart, D.A., Chen,Y-K. and Henline, W.D., "Effect of Non-Equilibrium Flow Chemistry and Surface Catalysis on Surface Heating to AFE," AIAA 91-1373, AIAA 26th Thermophysics Conference, June 24-26,1991, Honolulu, HI.

[15] Thompson, R.A.,"Three-Dimensional Viscous Shock-Layer Applications for the Space Shuttle Orbiter," *Thermophysical Aspects of Re-Entry Flows*,edited by J. N. Moss and C. D. Scott, Vol. 103 of Progress in Astronautics and Aeronautics, 1986, pp. 541-570.

[16] Tauber, M.E.,"A Review of High-Speed Convective, Heat Transfer Computation Methods," NASA TP 2914, July 1989.

[17] Candler, G.V. and MacCormack, R.W.,"The Computation of Hypersonic Ionized Flows in Chemical and Thermal Nonequilbrium," AIAA Paper 88-0511, 1988.

[18] Gnoffo,P.A.,"Point-Implicit Relaxation Strategies for Viscous, Hypersonic Flows," *Computational Methods in Hypersonic Aerodynamics*, edited by T.K.S. Murthy, Computational Mechanics Publications, Kluwer Academic Publishers, Hingham, MA,1991,pp. 115-151.

[19] Coakley, T.B.,"Implicit Upwind Method for the Compressible Navier-Stokes Equations," AIAA Paper 83-1958, July 1983.

[20] Weilmuenster, K.J., Gnoffo, P.A. and Greene, F.A.,"Navier-Stokes Simulations of Orbiter Aerodynamic Characteristics Including Pitch Trim and Bodyflap," *Journal of Spacecraft and Rockets*, Vol. 31, No. 3, May-June 1994, pp. 365-366.

[21] Gnoffo, P.A., Weilmuenster, K.J. and Alter, S.J.,"Multiblock Analysis for Shuttle Orbiter Re-entry Heating from Mach 24 to Mach 12," *Journal of Spacecraft and Rockets*, Vol. 31, No. 3, May-June 1994, pp. 367-377.

[22] Anon.,Access to Space, Advanced Technology Team, Final Report, Volumes 1-4, NASA, July 1993.

[23] Henline, W.D., Palmer, G.E., Milos, F.S., Olynick, D.R. and Chen, Y.-K.,"Aerothermodynamic Heating Analysis and Heatshield Design of an SSTO Rocket Vehicle for Access-to-Space," AIAA Paper 95-2079, 30th AIAA Thermophysics Confernce, June 19-22,1995, San Diego, CA.

[24] McGrory, W.D., Slack, D.C., Applebaum, M.P. and Walters, R.W., GASP Version 2.2, User's Guide, Aerosogt, Inc., 1872 Pratt Dr. Suite 1275, Blacksburg, VA 24060, 1993.

[25] Stewart, D.A.,Pallix, J. and Esfahani, L.,"Surface Catalytic Efficiency of Candidate Ceramic Thermal Protection Materials," NASA CDTM-20007, March 1995.

[26] Chen. Y.-K.,Henline, W.D. and Tauber, M.E.,"Mars Pathfinder Trajectory Based Heating and Ablation Calculations," *Journal of Spacecraft and Rockets*,Vol. 32, No. 2, pp. 225-230, MArch-April 1995.

[27] Nicolet, W.E. and Balakrishnan, A.,"Radiating Shock Layer Environment, RASLE, (User's Manual), Acurex Rept. UM-79-10/AS, Mountain View, CA, July 1979.

[28] Falanga, R.A. and Olstad, W.B.,"An Approximate Inviscid Radiation Flowfield Analysis for Sphere Cone Venusian Entry Vehicles," AIAA Paper 74-758, July 1974.

[29] Henline, W.D. and Tauber, M.E.,"Trajectory-Based Heating Analysis for the European Space Agency/Rosetta Earth Return Vehicle," *Journal of Spacecraft and Roclets*, Vol. 31, No.3, pp. 421-428, May-June 1994.

[30] Anon.,"Aerotherm Charring Material Thermal Response and Ablation Program, (CMA87S)," Acurex Report UM-87-13/ATD, Mountain View ,CA, Nov. 30,1987.

[31] Chen, Y.-K. and Milos, F.S.,"Solution Strategy for Thermal Response of Nonablating Thermal Protection System Materials at Hypersonic Speeds," AIAA 34th Aerospace Sciences Meeting , Reno,NV, January 1996.

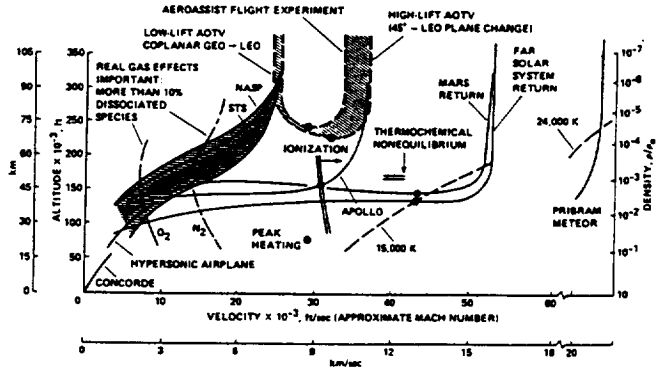

Figure 1. Comparison of vehicle flight regimes in Earth's atmosphere. (Ref.-5)

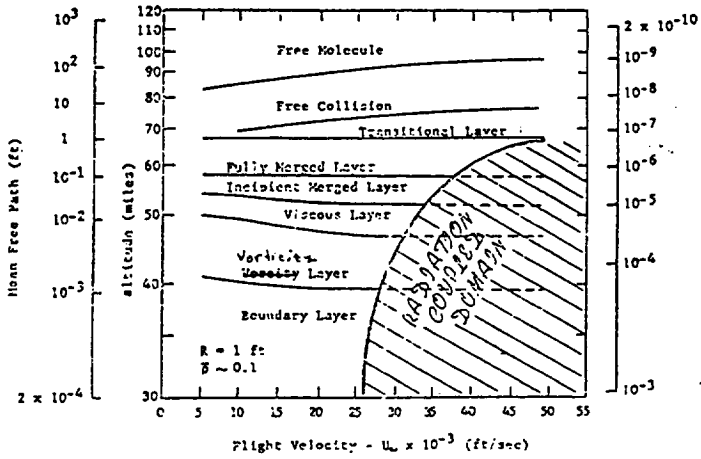

Figure 2. Flight regimes (based on Ref.-6 and modified from Ref.-7).

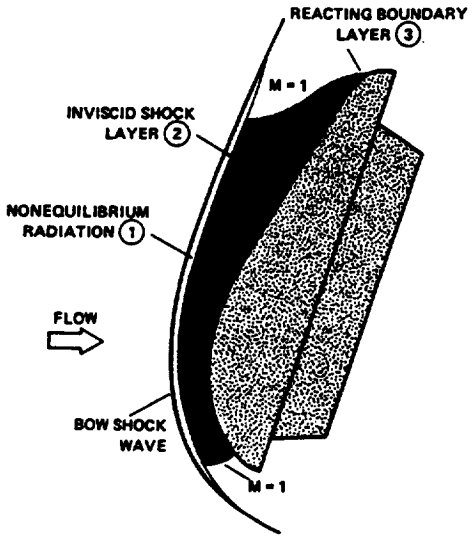

Figure 3. Vehicle geometry and flowfield characteristics of the AFE. (Ref.-14)

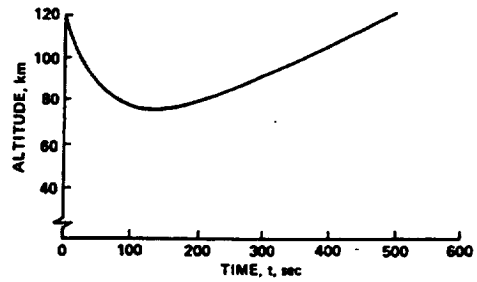

Figure 4. AFE trajectory. (Ref. 14)

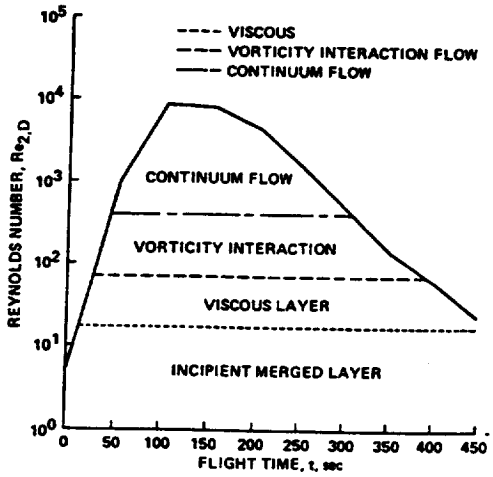

Figure 5. Reynolds number history and flight regimes for AFE. (Ref. 14)

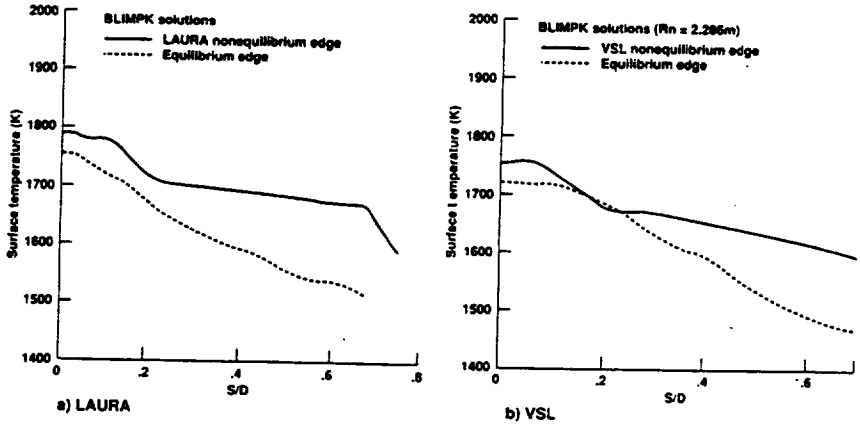

Figure 6. AFE surface temperature distribution showing effects of boundary layer edge conditions. (Ref. 14)

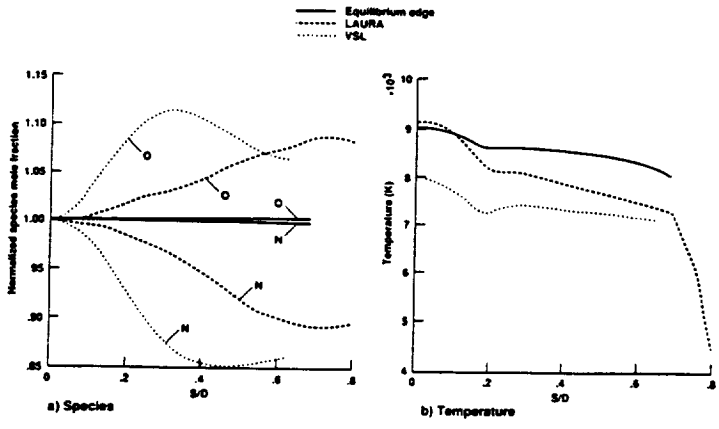

Figure 7. Comparison of boundary layer edge conditions for different computational methods applied to AFE. (Ref. 14)

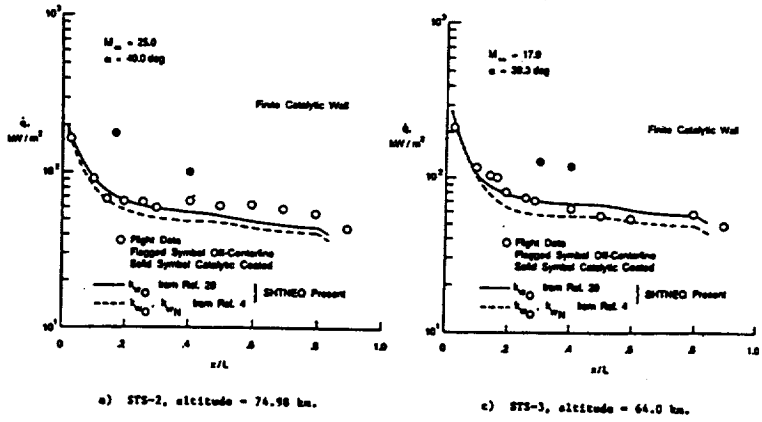

Figure 8. Viscous shock layer non-equilibrium heat transfer predictions for the Shuttle Orbiter windward centerline. (Ref. 15)

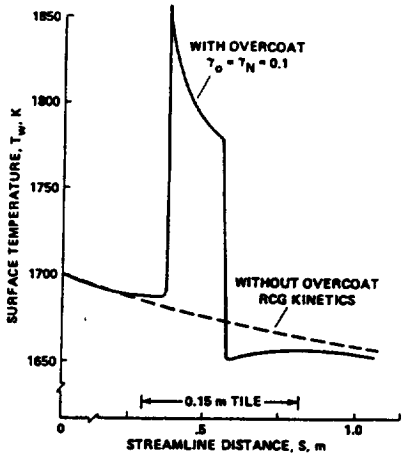

Figure 9. Surface temperature profile for the Wall Catalyis Experiment on AFE. (Ref. 13)

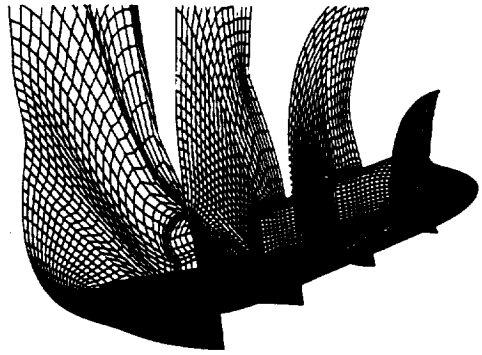

Figure 10. Shuttle Orbiter surface and volume grid (LAURA Code). (Ref. 20)

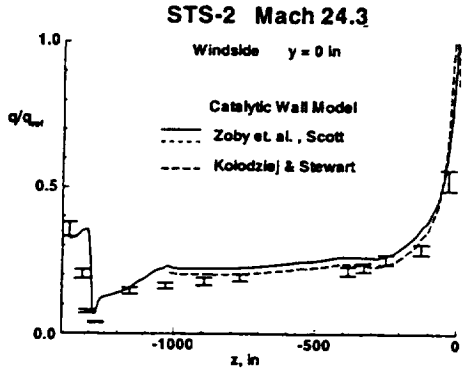

Figure 11. Surface heat transfer distribution for Shuttle windward centerline with surface catalysis. (Ref. 21)

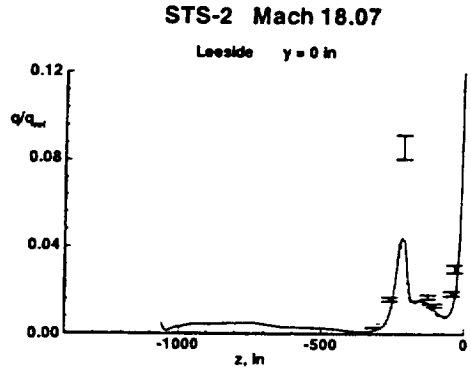

Figure 12. Leeward centerline surface heat transfer distribution for Shuttle. (Ref. 21)

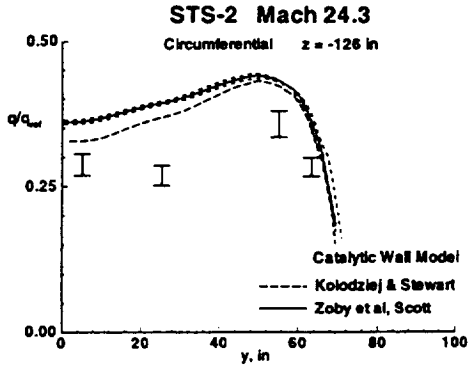

Figure 13. Windward circumferential heating distribution for Shuttle, 126 in. aft of nose. (Ref. 21)

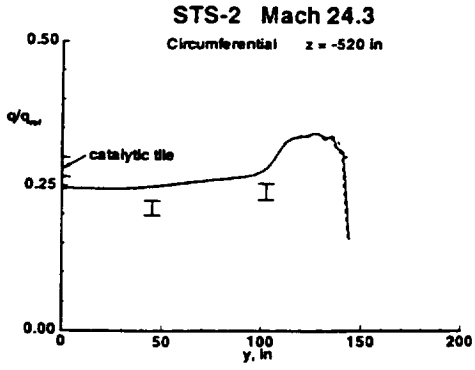

Figure 14. Windward circumferential heating distribution for Shuttle, 520 in. aft of nose. (Ref. 21)

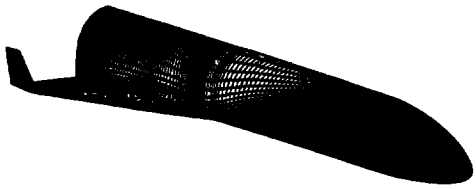

Figure 15. Langley Research Center SSTO(R) configureation and surface grid. (Ref. 23)

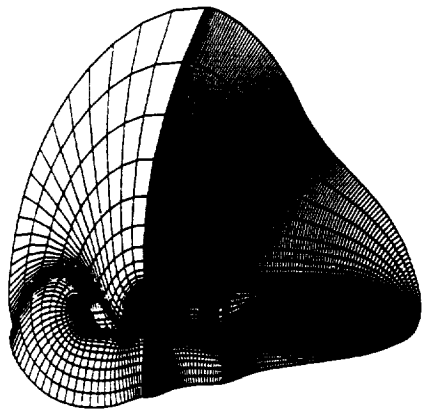

Figure 16. LaRC SSTO(R) finite volume flow grid (161 X 65 X 38) cells. (Ref. 23)

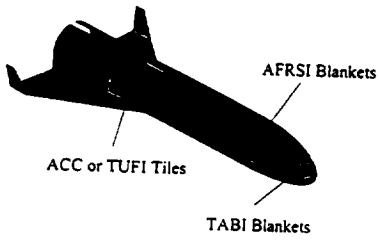

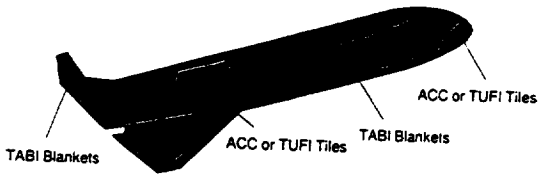

Figure 17. TPS material mapping for SSTO(R). (Ref. 23)

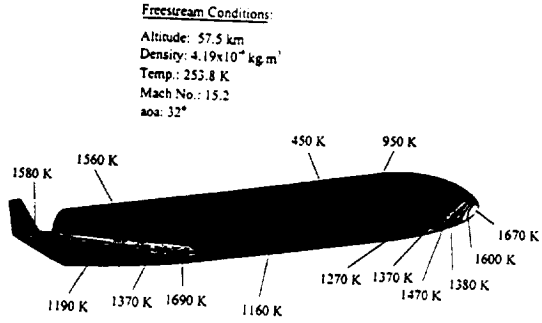

Figure 18. Adiabatic surface equilibrium temperatures for SSTO(R) at peak heating-laminar flow. (Ref. 23)

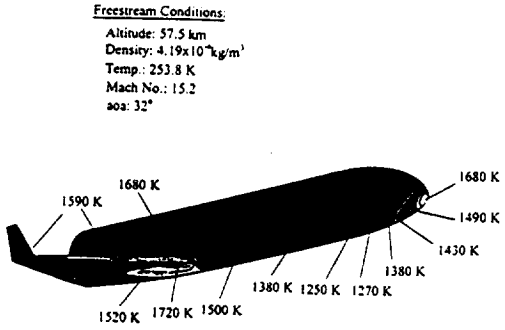

Figure 19. Adiabatic surface equilibrium temperatures for SSTO(R) at peak heating-turbulent flow. (Ref. 23)

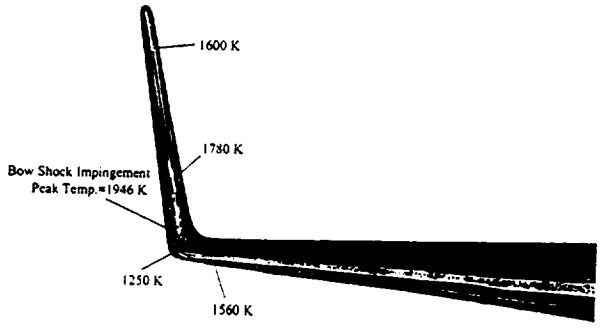

Figure 20. SSTO(R) winglet detail of maximum vehicle surface temperatures. (Ref. 23)

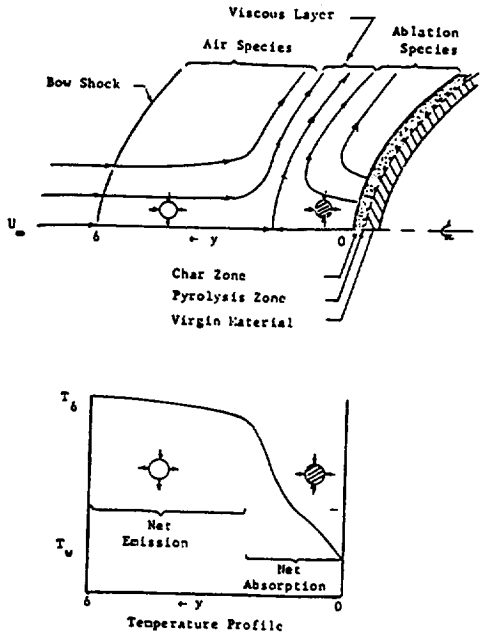

Figure 21. Schematic of various regions in a radiation/ablation coupled shock layer. (Ref. 8)

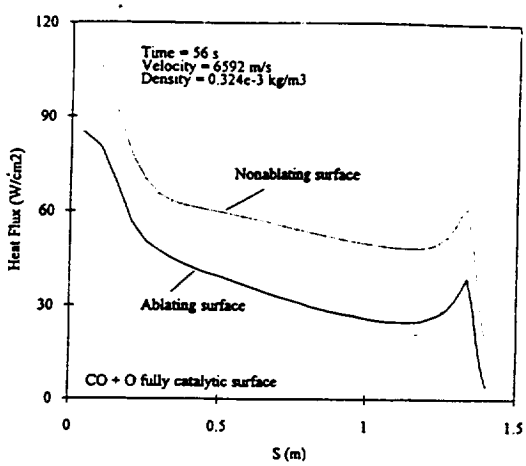

Figure 22. Surface convective heat transfer distribution for Mars Pathfinder forebody. (Ref. 26)

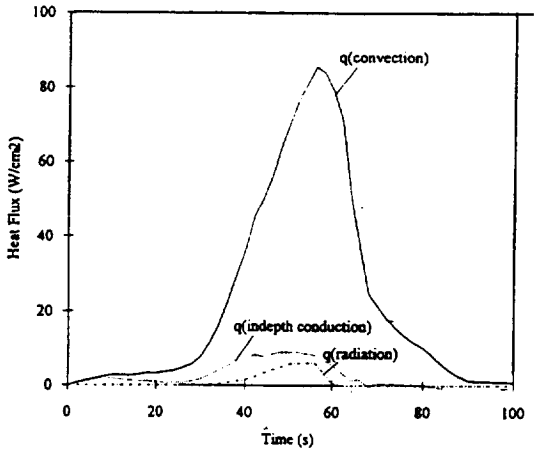

Figure 23. Mars Pathfinder stagnation point surface heat flux history. (Ref. 26)

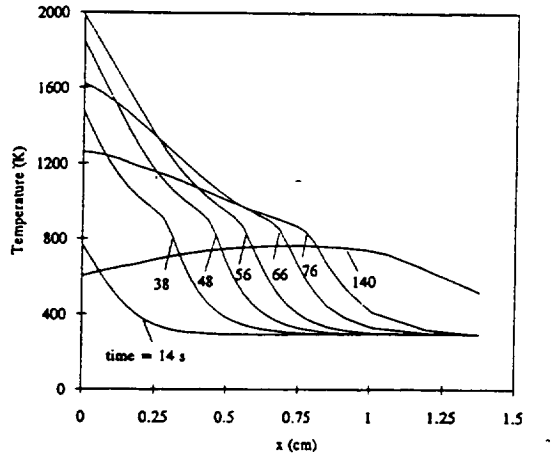

Figure 24. Mars Pathfinder stagnation point in-depth temperature histories. (Ref. 26)

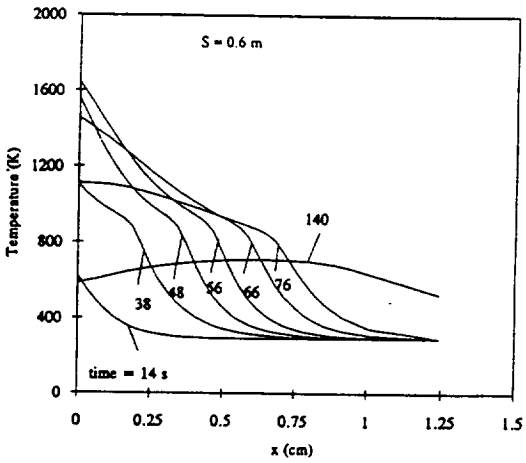

Figure 25. Mars Pathfinder downstream in-depth temperature histories. (Ref. 26)

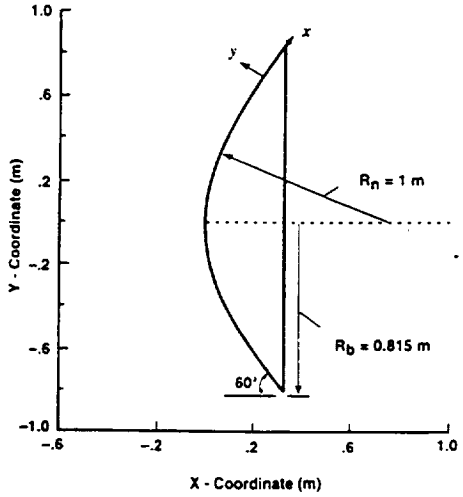

Figure 26. ESA/Rosett comet nucleus sample return probe forebody geometry. (Ref. 29)

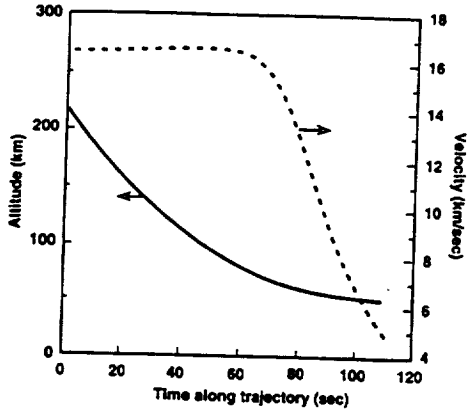

Figure 27. ESA/Rosetta entry trajectory. (Ref. 29)

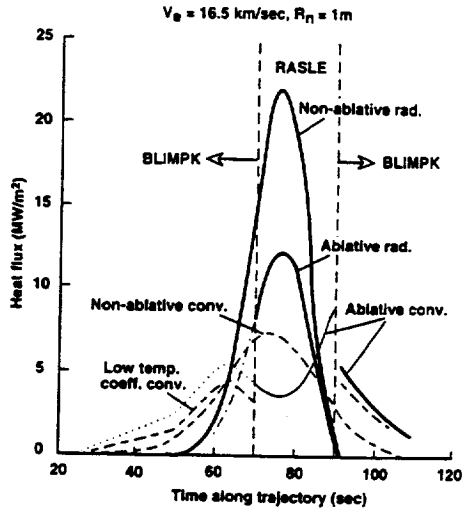

Figure 28. ESA/Rosetta stagnation heating. (Ref. 29)

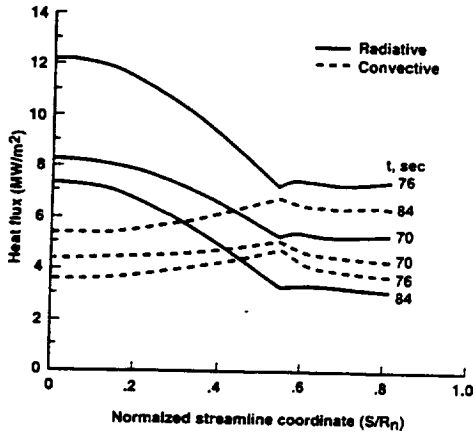

Figure 29. ESA/Rosetta probe forebody heating rate distributions. (Ref. 29)

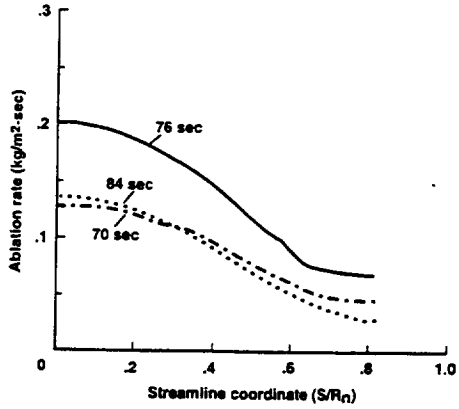

Figure 30. Forebody ablation rates for the ESA/Rosetta probe. (Ref. 29)

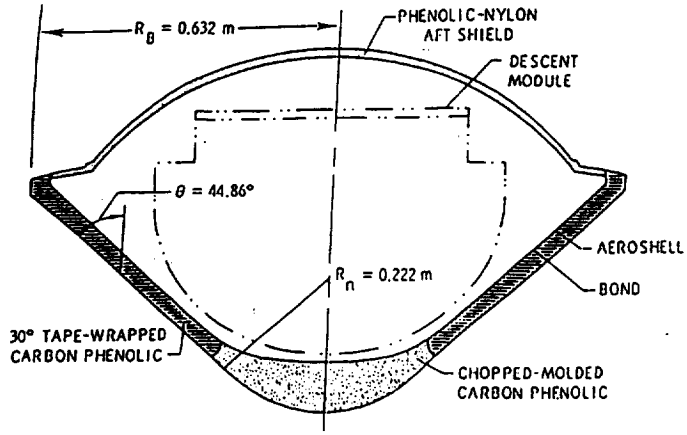

Figure 31. Galileo entry probe geometry.

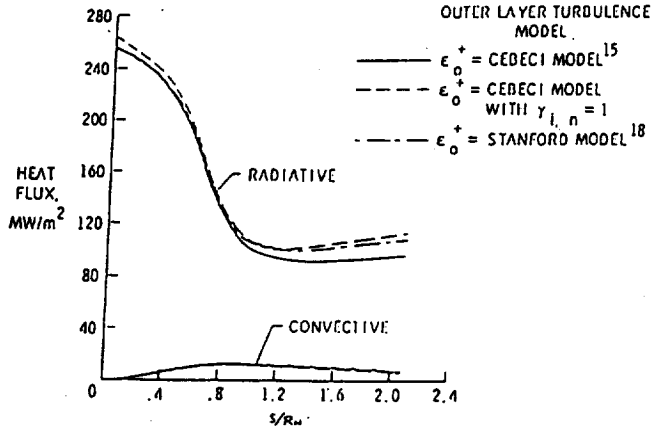

Figure 32. Galileo probe forebody heat transfer distributions.

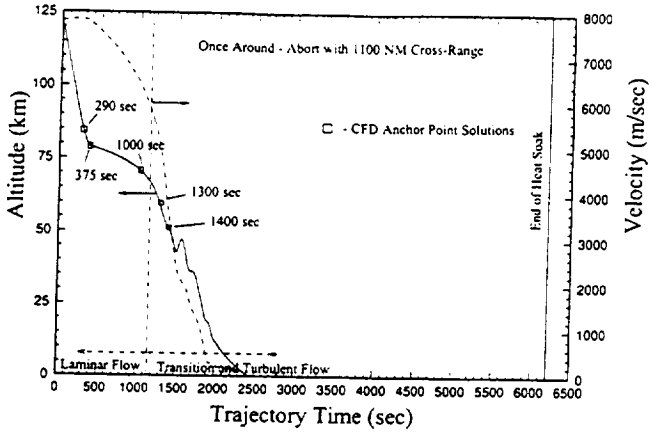

Figure 33. SSTO(R) entry trajectory and CFD anchor points. (Ref. 23)

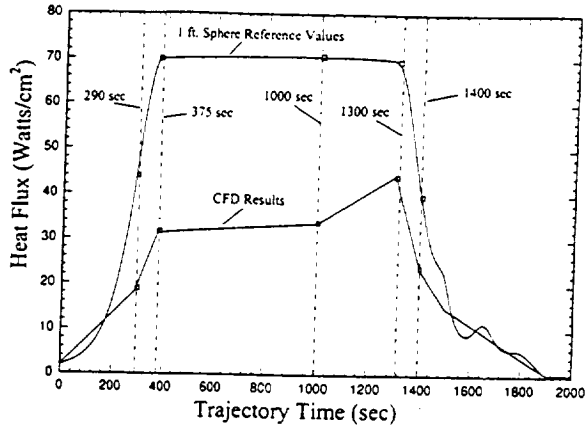

Figure 34. SSTO(R) stagnation point heat fluxes. (Ref. 23)

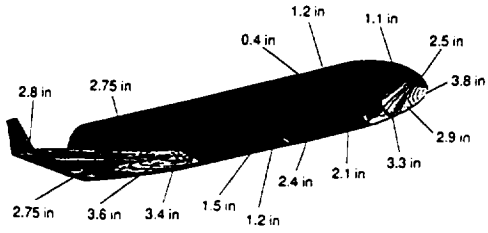

Figure 35. Contour plot of TPS thicknesses for SSTO(R) (Ref. 23)

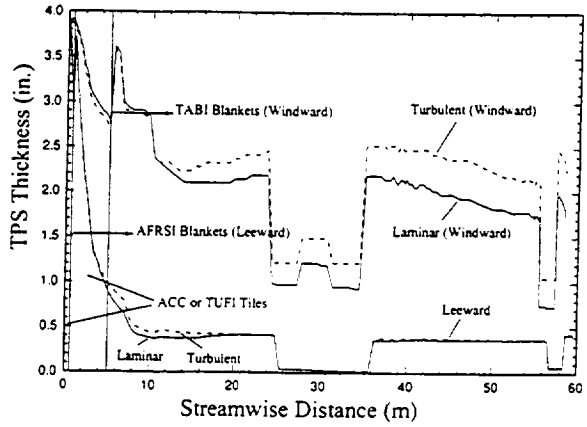

Figure 36. SSTO(R) centerline TPS thicknesses. (Ref. 23)

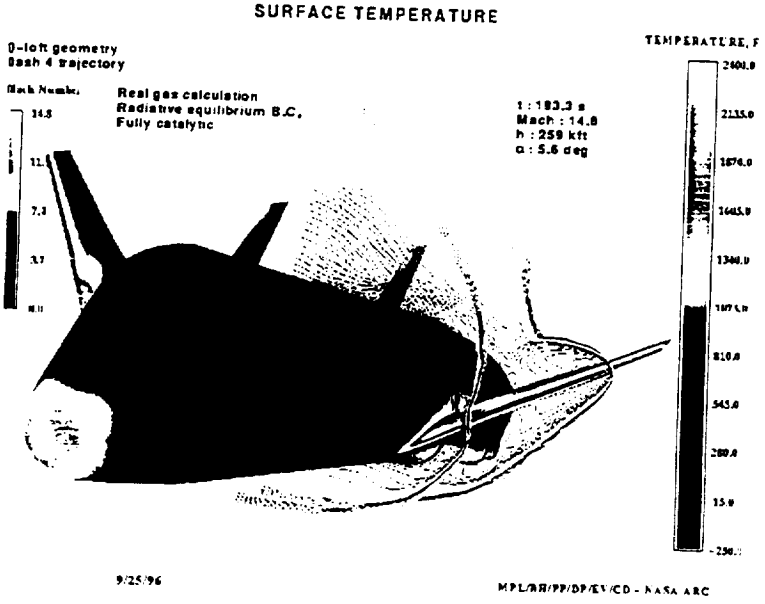

Figure 37. GASP solution for X33.

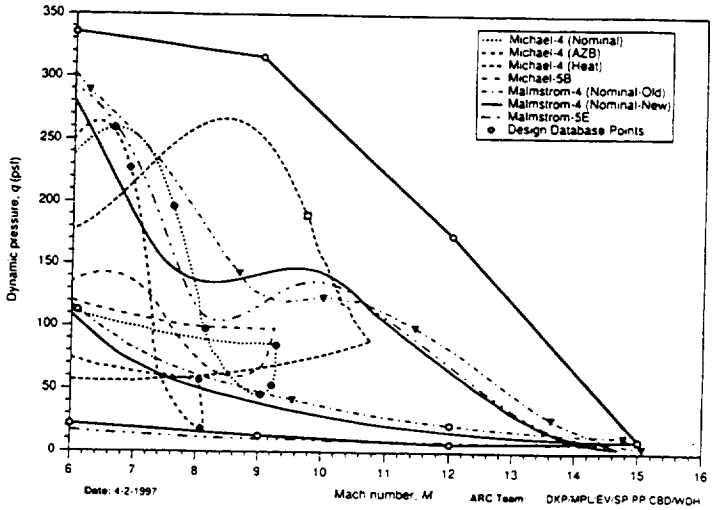

Figure 38. X33 CFD database/trajectory plot.

REPORT DOCUMENTATION PAGE

Form Approved
OMB No. 0704-0188

1. AGENCY USE ONLY *(Leave Blank)*	2. REPORT DATE	3. REPORT TYPE AND DATES COVERED
	September 1997	Conference Publication

4. TITLE AND SUBTITLE
Eighth Annual Thermal and Fluids Analysis Workshop on Spacecraft Analysis and Design

5. FUNDING NUMBERS

6. AUTHOR(S)
Editors and Co-chairs: Todd Peters, John Saiz, Dr. Carl Scott and Dr. Eugene Ungar, NASA/JSC

7. PERFORMING ORGANIZATION NAME(S) AND ADDRESS(ES)
Lyndon B. Johnson Space Center
Houston, TX 77058

8. PERFORMING ORGANIZATION REPORT NUMBERS
S-831

9. SPONSORING/MONITORING AGENCY NAME(S) AND ADDRESS(ES)
National Aeronautics and Space Administration; Washington, D. C. 20546

10. SPONSORING/MONITORING AGENCY REPORT NUMBER
NASA CP 3359

11. SUPPLEMENTARY NOTES

12a. DISTRIBUTION/AVAILABILITY STATEMENT
Available from the
NASA Center for Aerospace Information
800 Elkridge Landing Road
Linthicum Heights, MD 21090
Subject Category: 34

12b. DISTRIBUTION CODE

13. ABSTRACT *(Maximum 200 words)*

This document contains papers presented at the Eighth Annual Thermal and Fluids Analysis Workshop (TFAWS) on Spacecraft Analysis and Design hosted by the NASA/Johnson Space Center (JSC) on September 8-11, 1997, and held at the University of Houston - Clear Lake (UHCL) in the Bayou Building. The Workshop was sponsored by NASA/JSC. Seminars were hosted and technical papers were provided in fluid and thermal dynamics. Seminars were given in GASP, SINDA, SINAPS Plus, TSS, and PHOENICS. Seventeen papers were presented.

14. SUBJECT TERMS	15. NUMBER OF PAGES	16. PRICE CODE
cyogenics; environment, orbital thermal; flow fields, plume; catalycity; flow, hypersonic; radiation, thermal; analysis, aerothermal, thermal, structural, fluid	175	

17. SECURITY CLASSIFICATION OF REPORT	18. SECURITY CLASSIFICATION OF THIS PAGE	19. SECURITY CLASSIFICATION OF ABSTRACT	20. LIMITATION OF ABSTRACT
Unclassified	Unclassified	Unclassified	Unlimited